A Fluid Dynamics Approach to Bioreactor Design for Cell and Tissue Culture

Jonathan Dusting, John Sheridan, Kerry Hourigan

Fluids Laboratory for Aeronautical and Industrial Research (FLAIR), Department of Mechanical Engineering, PO Box 31, Monash University, Melbourne 3800, Australia; telephone: +61 3 9905 4913; fax: +61 3 9905 1825; e-mail: John.Sheridan@eng.monash.edu.au

Abstract: The problem of controlling cylindrical tank bioreactor conditions for cell and tissue culture purposes has been considered from a flow dynamics perspective. Simple laminar flows in the vortex breakdown region are proposed as being a suitable alternative to turbulent spinner flask flows and horizontally oriented rotational flows. Vortex breakdown flows have been measured using three-dimensional Stereoscopic particle image velocimetry, and non-dimensionalized velocity and stress distributions are presented. Regions of locally high principal stress occur in the vicinity of the impeller and the lower sidewall. Topological changes in the vortex breakdown region caused by an increase in Reynolds number are reflected in a redistribution of the peak stress regions. The inclusion of submerged scaffold models adds complexity to the flow, although vortex breakdown may still occur. Relatively large stresses occur along the edge of disks jutting into the boundary of the vortex breakdown region. © 2006 Wiley Periodicals, Inc.

Keywords: bioreactor technology; fluid dynamics; particle image velocimetry; cell culture; scale-up

INTRODUCTION

Improving the outcomes of cell and tissue culture through the use of bioreactors is a goal that has recently received substantial research interest (Darling and Athanasiou, 2003; Freed and Vunjak-Novakovic, 2000; Martin et al., 2004; Shachar and Cohen, 2003). This has partly been generated by strong advancements in the fields of tissue engineering and cell culture based research. In particular there is now the need to produce therapeutically relevant cell yields or tissue constructs on a scale that goes far beyond what is typically required for laboratory use (Carrier et al., 1999; Martin et al., 2004; Wu et al., 1999). Cell culture bioreactors range from, among other designs, highly specialized microscale perfused vessels (Nielsen, 1999; Niklason et al., 1999), to larger rotating wall annular flow vessels (Begley and Kleis, 2000, 2002; Freed and Vunjak-Novakovic, 1995, 2000; Goodwin

et al., 2003; Kleis et al., 1990), to simple upright tanks stirred either by impeller or magnetic stirrer (Cherry and Papoutsakis, 1986; Leckie et al., 1991; Kallos et al., 1998; Vunjak-Novakovic et al., 1996). Bioreactor design requirements are numerous and varied, and include hydrodynamic stress conditions, nutrient delivery, gas transfer, sterility, heat transfer, and maintenance. Where adherent cells (e.g., endothelial cells, epithelial cells, or chondrocytes) are cultured, surface properties and the flow around bluff bodies also become important.

The process of generic bioreactor design is impeded by the range of hydrodynamic requirements, which vary on a case-by-case basis. For example, different phenotypes will respond in different ways to a certain shear exposure. Furthermore, in the case of cell culture for tissue engineering purposes, a high cell yield and a complex aggregate structure may be required. These complications limit mammalian cell bioreactor technology, as the expertise of the cell culturer rarely encompasses all the disciplines necessary to adequately meet all the design requirements. Consequently, the fluid dynamics of the system is one area that has lacked thorough attention. Despite a few attempts to predict bioreactor flows using both experimental and computational fluid dynamics (Begley and Kleis, 2000, 2002; Curran and Black, 2004; Sucosky et al., 2004; Venkat et al., 1996; Williams et al., 2002), there are relatively few recorded cases where the hydrodynamic force considerations have been given prominence.

The approach usually exercised in the previous bioreactor fluid dynamics studies has been to commence with a measurement or adaptation of an established bioreactor technology. Our approach proceeds from a different angle, with an investigation of more fundamental flows derived as idealizations of mixed flask bioreactor flows. The intention is to demonstrate that appropriate shear and mixing conditions can be better located within flows using a spatially resolved three-component velocimetry technique. A wider aim is to demonstrate the merits of characterizing bioreactor flows in terms of independent, non-dimensional parameters. By linking models that describe the manner in which the internal physical properties are determined by certain input

conditions, with models of how the cell and tissue behavior are mediated by these physical properties, there is the potential to drastically improve application-based bioreactor design and selection procedures.

The chosen vessel configuration is that of a vertically oriented cylinder with a rotating bottom and a free surface. In our chosen model, the diameter of the rotating bottom matches that of the stationary cylinder, and the remainder of the cylindrical working section is devoid of protruding objects that might disturb the flow. The free surface is included to enable natural gas transfer to the cell culture medium. The primary reason this geometry has been selected is that it has the simplicity of the spinner flask, without the overly complex turbulent flow that results under typical user conditions (Sucosky et al., 2004). Having control over the flow ensures repeatability of the hydrodynamic conditions to which cells are exposed. Another important benefit is that the laminar flows produced in these vessels have a strong secondary recirculation pattern as well as the potential for a third, low-stress recirculation region to occur on the central axis. The phenomenon that produces this region is known as Vortex Breakdown (VB). While being a novel concept at present, the introduction of VB to bioreactor flows is likely to be a favorable step. The successful incorporation of VB into industrial flame control processes (see review by Ishizuka (2002)) illustrates its potential to be used as a mixing control mechanism in swirling flow applications. However, in order to be successfully applied to cell culture mixing vessels, the VB phenomenon requires further investigation in terms of properties relevant to the application, such as local stress conditions and the relationship between the VB region and the remainder of the flow. In the current article, both of these aspects are addressed.

Flows within bottom-driven cylinders with a free-surface are typically classified within the fluid dynamics literature in terms of their Reynolds Number, $Re = \omega R^2 / \nu$, and the vessel aspect Ratio H/R, where ω represents the angular speed of the disk, R is the radius of the working section, H is the fluid depth, and ν is the kinematic viscosity. Re represents the degree to which inertial forces dominate viscous forces. Using dimensionless parameters such as these means that flow measurements can be scaled with a change in vessel properties. Scalability, which seems to have been overlooked during previous, more specialized, bioreactor design processes, is important in the context of the growing need to produce bioreactors capable of larger yields.

When the disk is rotated at constant speed, angular momentum is imparted to the fluid within the cylinder, causing a flow which is predominately azimuthal. The resulting flow in the radial and axial directions is relatively weak compared to the azimuthal flow, however, it constitutes the key mechanism for both fluid mixing and internal shearing, and so is of great interest to this study. At lower Reynolds numbers ($Re < 780$, for $H/R = 1.5$), the meridional plane flow is a straightforward recirculation pattern, with axial flow near the wall ($r/R \rightarrow 1$), where r is the radial position from the centerline, in the direction of the free-surface, axial flow near the axis of symmetry ($r/R \rightarrow 0$) in the direction of the bottom disk, and radial flow near the cylinder ends. At higher Re, but still in the laminar regime ($Re = 780$, for $H/R = 1.5$), a profound change in flow topology occurs. Forming along the central axis of symmetry is a VB bubble similar to that observed in various swirling flows (Billant et al., 1998; Escudier, 1988; Hall, 1972; Sarpkaya, 1971). As Re increases, different VB patterns develop, depending on H/R. Other available literature describes this flow development in more detail (Brøns et al., 2001; Lopez and Marques, 2004; Spohn et al., 1993). In general, the VB region is characterized by its bubble-like nature, consisting of one or more stationary or slowly oscillating pockets of enclosed fluid located on the axis of symmetry. The motion of fluid within VB bubbles is yet to be definitively described, although there have been attempts to simulate inner-bubble particle trajectories for the case where the free surface is replaced by a fixed lid (Sotiropoulos and Ventikos, 2001; Sotiropoulos et al., 2002).

Studies of the flow in free-surface cylindrical containers with rotating bottom disks are relatively rare compared with the closed cylinder case. Spohn et al. (1993) characterized the VB states for the free-surface case in terms of Re and H/R. While they observed VB bubbles for a similar range of Re and H/R to the fixed lid case (Escudier, 1984), the topologies of the various flow regimes were found to differ significantly. In particular, for the free-surface case the absence of a no-slip boundary layer allows the vortex breakdown region to attach to the surface. The right-hand side meridional plane flow corresponding to the case where the VB region is attached to the free surface is schematized in Figure 1. The locations of the separate flow regions are highlighted by different shading.

This article describes experimental studies undertaken in a specially constructed physical rig designed to replicate the flow described above, with and without the addition of stationary scaffold models. Laser-particle flow visualization has been used to observe the full-field flow pattern and to compare the flow development with previous observations.
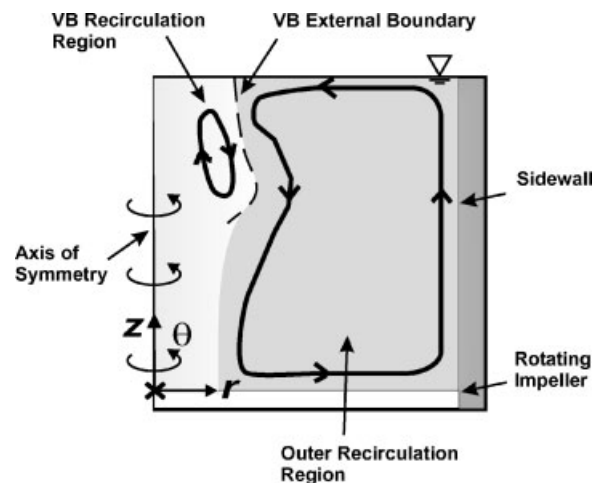
Figure 1. Annotated schematic of the vortex breakdown flow pattern in the meridional plane. The two separate flow regions are shaded differently.

Stereoscopic particle image velocimetry (SPIV) has been used to measure dynamic properties especially relevant to cell culture, in particular the velocity field in the secondary flow plane and the three-dimensional (3D) stress field. It is only with 3D measurement techniques that these properties can be adequately quantified for this flow. As mentioned by Humphrey (2001), the quantification of stresses relevant to cell mechanics in terms of 3D principal stresses is highly preferable to the more common practice of characterizing stress fields by the measurement of two-dimensional shear or, broader still, by a single global parameter (Sinskey et al., 1981; Vunjak-Novakovic et al., 1996).

METHODS

Experimental Model

As shown in Figure 2, the experimental model consisted of a polished transparent container with a 65 mm diameter drilled center hole, mounted onto a stainless steel base. The square exterior faces of the block were kept flat in order to reduce refraction effects that result in optical distortion errors during the use of image-based measurement techniques. The scale was kept similar to that of mammalian cell bioreactor devices found in the literature, which typically have a fluid volume of around 100–300 mL. The top surface was left open during experiments to allow scaffolds to be suspended in the working section. Careful rig assembly was necessary to diminish the misalignments and artificial perturbations that have been shown to influence the VB structure (Thompson and Hourigan, 2003). A flat, circular disk acted as the rotating bottom, and was screwed to a drive-shaft assembly which was located in the center of the base, as illustrated in Figure 2. The shaft was rotated by a small stepper motor (Sanyo–Denki SD17) run through a high-performance motion controller (National Instruments Australia, North Ryde, NSW, Australia), enabling 5.12×10^4 steps per revolution. The angular velocity of the disk was measured independently using a photonic sensor system (MTI Instruments, Albany, NY) and was found to be accurate to within $\pm 0.1\%$. Good mixing and the use of a small fluid volume (161.8 mL)

Table I. List of bioreactor dimensions, operating conditions, and fluid properties.

Parameter	Symbol	Experimental domain
Cylinder radius (mm)	R	32.5
Free surface height (mm)	H	48.8
Fluid volume (mL)	V	162
Impeller rotational speed (rpm)	ω	5.96–27.34
Fluid kinematic viscosity ($\times 10^6 \, \text{m}^2/\text{s}$)	ν	1.08–1.09
Fluid density (kg/m³)	ρ	999
Fluid temperature (°C)	T	17.0–17.5
Scaffold radius (mm)	R_s	2.5–7.5
Scaffold thickness (mm)	t_s	1–3
Scaffold needle radius (mm)	r_n	0.5
Height ratio	H/R	1.5
Reynolds number	Re	600–2800
Scaffold radius	r_s/R	0.08–0.23
Scaffold aspect ratio	t_s/r_s	0.4

reduced the thermal gradients across the working section. The base and motor bracket both screwed directly onto a precision flat optical table in a manner that ensured accurate assembly and minimal mechanical vibration. Re accuracy was limited primarily by slight fluctuations in fluid temperature; however, it could be controlled to within 1.4%. Table I represents a list of parameter values used during the current investigation.

The co-ordinate system is illustrated in the inset of Figure 2. The axes are defined cylindrically, that is, by radial (r), axial (z), and angular (θ) position. The origin corresponds to the top center of the rotating disk. Positional data were typically normalized by cylinder radius, R, in the radial direction and surface height, H, in the axial direction. The surface condition during lid rotation was verified using zoom and video photography. Aside from wetting very close to the water–solid interface, no deformation was observed. Indeed, Spohn et al. (1993) also reported negligible deformation, despite having a much larger Froude number ($\sim 10^0$, compared to $\sim 10^{-2}$ in the present study). For the majority of the experimental cases, H/R was kept constant at 1.5, measured to an accuracy of 0.02% using a height gauge (Mitutoyo Corporation, Japan). This value was chosen because it represents a case for which vortex breakdown occurs over a large Re range; however, a more optimal height ratio may be located by conducting additional characterizations. As a comparison, Vunjak-Novakovic et al. (1996) used $H/R = 1.05$ and Sucosky et al. (2004) used $H/R = 1.17$.

The experimental scaffold models consisted of a disk and a supporting column. The disks were cylindrical in shape with a circular cross-section, a thickness t_s, and a radius r_s. The disk aspect ratio, t_s/r_s, was held at 0.40. This represents a similar aspect ratio to that used by Williams et al. (2002) ($t_s/r_s = 0.35$), although it should be noted that Freed and Vunjak-Novakovic (2000), amongst others, used $t_s/r_s = 0.80$, while Botchwey et al. (2004) used $t_s/r_s = 1.25$. The disks were constructed from Perspex, and had non-compliant surfaces. Unlike tissue engineering scaffolds, which are porous in order to maximize the potential for extra-cellular matrix materials to penetrate between cells, the Perspex disks
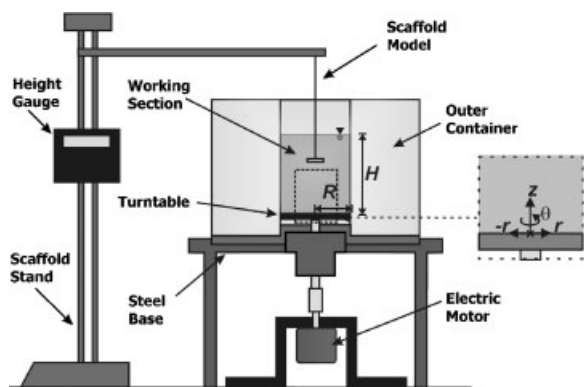
Figure 2. Annotated rig vertical cross-section, with scaffold placement system, co-ordinate system and relevant dimensions.

were 100% solid. However, due to the minuscule size of the scaffold pores, the effect of porous and non-porous objects on the bulk flow should be the same. The flow within the scaffold itself is beyond the scope of the current investigation, but for the study conducted by Botchwey et al. (2004) it was reported that the stresses associated with these flows were an order of magnitude lower than the external surface stresses. Sucosky et al. (2004) similarly used polymer disks to simulate the dynamic conditions around scaffolds. In order to investigate the effect of varying the scaffold to bioreactor radius ratio r_s/R, three disks were used. The radius of the smallest disk was 2.5 mm, and the dimensions of the other disks were multiples of this (5.0 mm and 7.5 mm). Therefore, the radius ratios investigated were $r_s/R = 1/13$, 2/13, and 3/13.

Flow Visualization

Flow visualization studies were conducted using a vertical light sheet to illuminate highly reflective particles seeded within the fluid. A particular emphasis was placed on visualizing particles following the motion of fluid within the VB bubble so that the geometry of this region could be easily distinguished. Fourteen-micrometer diameter polymer spheres (Vestosint) with a specific gravity of 1.05 were used as particles. The light sheets were created using either a 532 nm laser (Spectra-Physics) or a stage lamp. Laser was preferred, as it facilitated the formation, with the aid of precision lenses, of a 1 mm thick light sheet with minimal divergence. However, for cases involving a submerged scaffold, excessive specular reflection off the needle made laser particle visualization less effective, and so the laser sheet was replaced by a more diffuse white light sheet, generated by the stage lamp.

Stereoscopic Particle Image Velocimetry

SPIV was the primary tool used for quantitative flow measurement. The stereoscopic technique is an extension of traditional cross-correlation particle image velocimetry (PIV) that utilizes two, rather than one, cameras in order to measure three, rather than two, components of each velocity vector on a two-dimensional grid across a planar field. The necessity in this study to measure all three-velocity components arises mainly for two reasons. Firstly, the high ratio of out of plane (v_θ) to in-plane (v_r, v_z) velocity components in the measurement plane caused a relatively high perspective error in 2D PIV studies. Secondly, the capability to measure the third component of velocity added significant detail to the results. This was especially relevant to the present study, as one aim was to gain as much information as possible about the stresses acting within the fluid and along scaffold surfaces. It is only by deriving the full 3D deformation stress tensor, T, that the principal stresses can be determined. As the flow is nearly axi-symmetric, by assuming that the azimuthal gradients ($\partial v_w/\partial\theta$, $\partial v_z/\partial\theta$ and $\partial v_\theta/\partial\theta$) are negligible relative to the other gradients, it was possible to obtain an estimate of T.

During the past decade the use of SPIV has increased, and several articles have been written describing the process in detail (Prasad, 2000; Soloff et al., 1997; Willert, 1997). The configuration used during the current experiment is illustrated schematically in Figure 3. An angular displacement system was chosen, meaning that the two CCD cameras (PCO Imaging Pixelfly) were positioned at a fixed angle off center. Focus across the image plane was achieved by utilizing the Scheimpflüg condition, which involves rotating the camera's CCD array away from the camera lens. The displacement angle was 45°, chosen both for practicality and to restrict the errors associated with out of plane velocity measurement (Lawson and Wu, 1997; Prasad, 2000). Calibration was conducted using an in situ-located test block consisting of a 65 mm diameter half-cylinder with a sandblasted front plane. By back-illuminating the test block with the diffused white light sources shown in Figure 3, a speckle pattern could be viewed across the measurement plane, and recorded using the two cameras for the purposes of distortion mapping.

As with traditional two-dimensional PIV, SPIV relies on correlation between multiple particle images captured at a known time interval. For this study, 100 double-buffered image pairs were captured simultaneously on the angularly displaced cameras at a frequency of 4.64 Hz. Twelve micrometers diameter, silver coated, hollow glass microspheres (Potters Industries Pty Ltd, Melbourne, VIC, Australia) were used as tracer particles, and illuminated by a 1.5 mm thick light sheet powered by the 532 nm laser. Laser/camera synchronization was achieved using a specially designed timing box. Cross-correlation between image frames was conducted using in house software with an incorporated local-fit vector rejection and replacement algorithm. Subsequent processing was undertaken using a series of algorithms written using Matlab (Mathworks, Chatsworth, NSW, Australia). The SPIV results presented in this article were time-averaged over 100 frames for the sake of clarity, a process made feasible by the steady and nearly axi-symmetric nature of the flow.
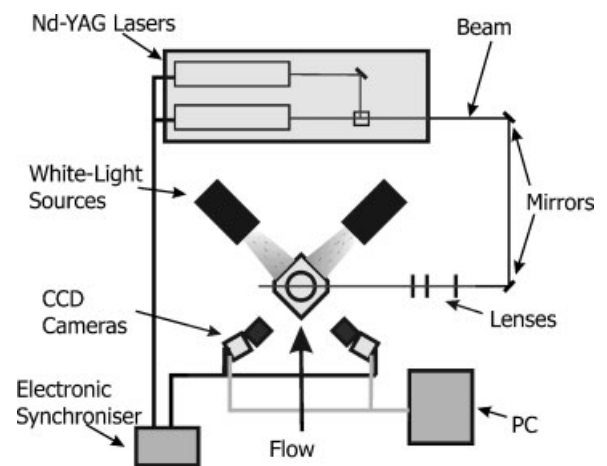
Figure 3. Annotated schematic of the SPIV configuration, viewed from above.

A 55 mm Nikkor lens (Nikon Corporation, Japan) was used to conduct SPIV measurements across $-0.96 \leq r/R \leq 0.96$, at separate axial positions corresponding to the upper and lower halves of the meridional plane. The two CCD cameras each had an image resolution of $1,360 \times 1,024$ pixels. With appropriate particle seeding (Raffel et al., 1998), the use of 50% window overlap, and recursive correlation window shifting (Hart, 2000), it was possible to obtain a measurement resolution of 96×50 vectors. For the scaffold cases, the number of obtainable vectors was reduced by light blockage and reflection caused by the supporting column. The spacing between vectors obtainable using SPIV was 0.02R.

A trial case involving solid body rotation of a test plate was carried out to verify the system's capability. The measured rotation angle was well within the accuracy of the spring micro-gauge used to set the $1.0°$ plate rotation angle. The standard deviations of the horizontal and vertical displacement were 0.23 and 0.09 pixels, respectively. Furthermore, stress fields derived using SPIV were validated by comparing them with stress fields derived by numerical simulation.

RESULTS AND DISCUSSION

Flow in Cell-Suspension Bioreactors

The effect of an increase in Re on flow topology can be broadly and qualitatively studied through flow visualization. The three images in Figure 4 present a vertical cross-section of the flow field across the cylinder diameter for three different values of Re chosen as examples of different flow topologies. Due to a long camera exposure time, the imaged particles appear as streaks. The near symmetry of the flow on either side of the cylinder indicates that the flow is approximately axi-symmetric. The majority of the particles are entrained near the perimeter of two recirculation regions. Digital adjustment of contrast levels and color inversion have been used to enhance the VB geometry in black and white. The larger recirculation is driven by a radial pumping from the boundary layer located at the bottom disk, otherwise known as the Ekman layer. The smaller recirculation located near the central axis of symmetry is within the vortex breakdown 'bubble'. For case (a), $Re = 780$, the VB region is much smaller than for cases (b) or (c), and has its upstream stagnation point on the axis. The range of Re values for which the bubble is located entirely on-axis is relatively small. The second image in Figure 4 provides an example, at $Re = 1,350$, of an expanded VB bubble that has attached upstream to the free surface. Once attached to the free surface, the outer boundary of the VB region moves radially outward as Re increases. The third and final photograph in Figure 4, taken at $Re = 1,920$, provides an example of a radially expanded bubble. At Re above this case, low frequency oscillations are apparent. These observations confirm the development described photographically by Spohn et al. (1993) and numerically by Brøns et al. (2001) for this aspect ratio. The close agreement between the flow structures observed at
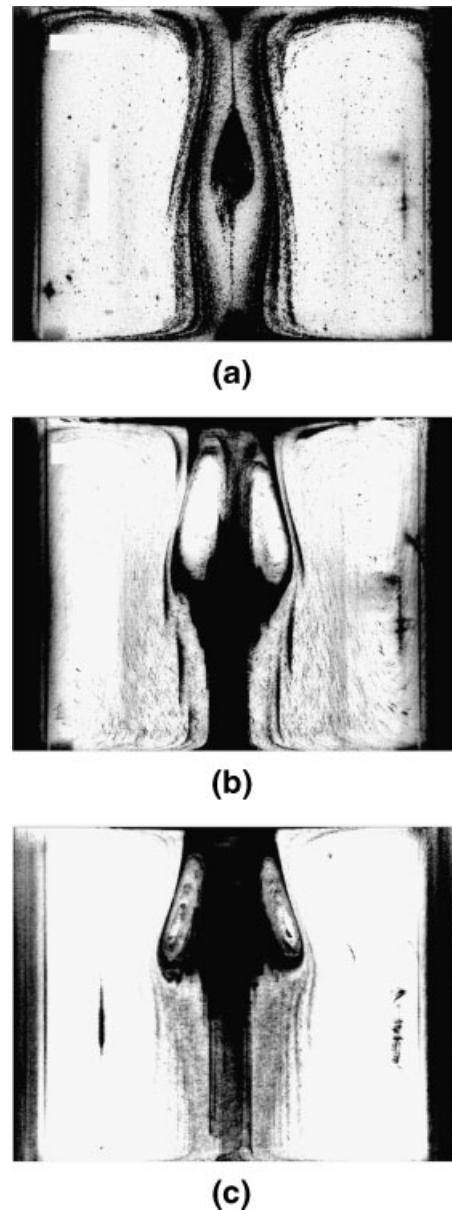
Figure 4. Laser-particle visualization of VB bubble geometry for (**a**) $Re = 780$, (**b**) $Re = 1,350$, and (**c**) $Re = 1,920$. Both the right-hand side and the left-hand side of the meridional plane are shown.

particular Re in this experiment and in previous studies instils confidence in our experimental set-up and provides some validation of our assumptions.

Of course, much more detailed information can be obtained from the quantitative measurements. Several plots illustrating the fluid kinematics are presented in Figures 5–9. Velocity fields in 3D vector form are shown in Figure 5 for Re values corresponding to (a), before the onset of vortex breakdown ($Re = 600$), and (b), the vortex breakdown regime ($Re = 1,200$). The measurements in the z domain are limited by the distorted nature of the SPIV field of view; however, a comparison of the region $0.4 \leq z/H \leq 1.0$ is sufficient to highlight the difference between the two cases. Because of the axi-symmetric nature of the flow, only one half of the cylinder ($r/R \geq 0$) is presented. Despite the restricted field of
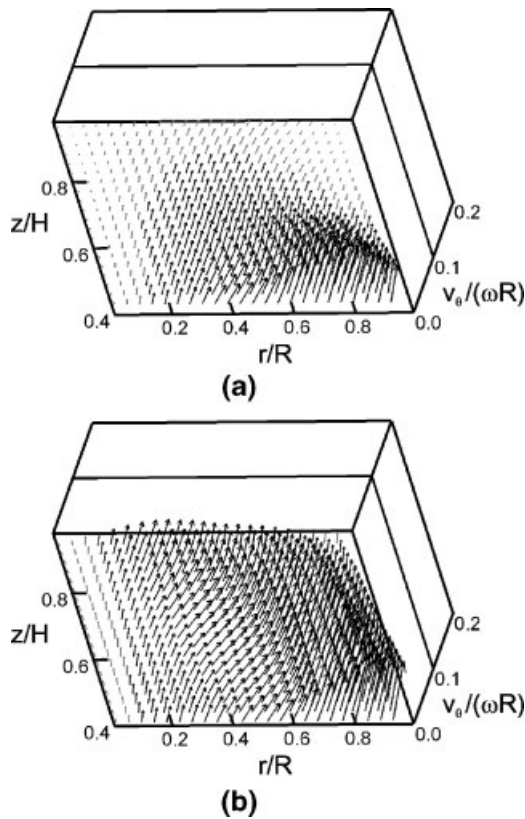
Figure 5. Three-dimensional vector fields across part of the meridional plane at (**a**) $Re = 600$, and (**b**) $Re = 1,200$. The right-hand side of the plane is shown, and the vector shading represents levels of azimuthal velocity component (v_θ).

view, both plots exhibit a large dynamic range across the measurement region. At $Re = 600$, there is insufficient momentum imparted on the fluid by the rotating disk to cause significant fluid motion above $z/H \approx 0.7$. The fluid that is in motion is relatively easier to visualize three-dimensionally than that at $Re = 1,200$. In the latter case, there is enough inertia supplied by the disk to cause a 3D recirculation pattern through the entire vessel. The distribution of local velocity is
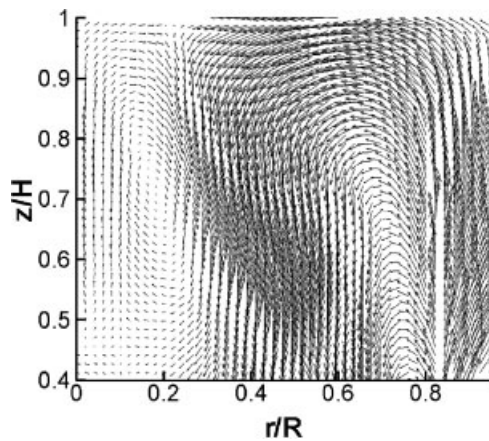

Figure 6. Two-dimensional (v_r, v_z) vector fields across part of the meridional plane at $Re = 1,200$. The right-hand side of the plane is shown.
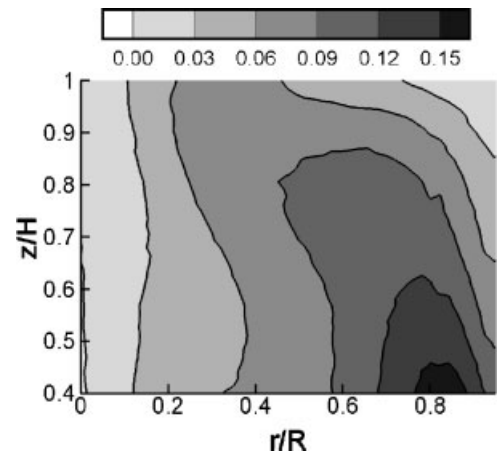

Figure 7. Contours of azimuthal velocity (v_θ) across part of the meridional plane at $Re = 1,200$. The right-hand side of the plane is shown. The magnitudes are normalized by (ωR).

more irregular than at $Re = 600$. For instance, the direction and magnitude of the spiraling motion changes several times across the field of view, whereas the recirculating motion at $Re = 600$ is relatively straightforward. The vortex breakdown region is not entirely clear in Figure 5, but is contained within the slower fluid region near the axis. While the 3D vector fields illustrate the flow in general terms, a more thorough understanding is gained by breaking the data down to plots that are easier to conceptualize.

Figure 6 illustrates the velocity vector field resolved in the meridional plane, while Figure 7 represents contours of the third velocity component, v_θ, for the same case ($Re = 1,200$). Both plots are extracted from the same measurement set as Figure 5b, and in both cases the velocity field is normalized by the disk tip speed $R\omega$. In contrast to Figure 5b, the vortex breakdown bubble is easily distinguished in the 2D vector plot. It is clear, for instance, that there is a separate, near-axis recirculation region centered at (r/R, z/H) = (0.2, 0.7), and
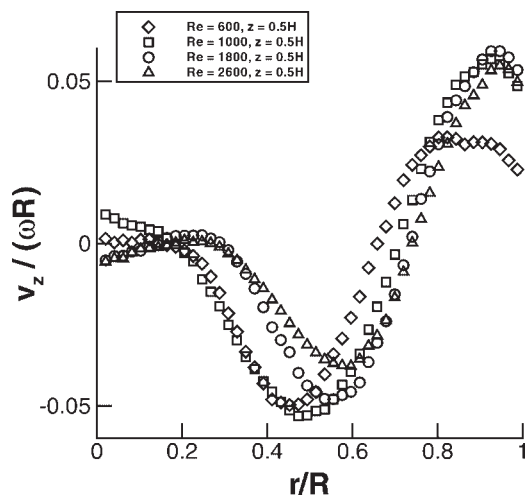
Figure 8. v_z profiles across the cylinder radius at $z/H = 0. 5$. Different Re cases are represented by different symbol shapes, as denoted in the legend.
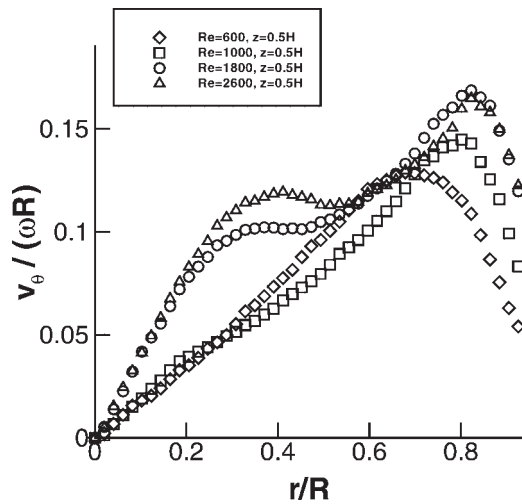
Figure 9. v_θ profiles across the cylinder radius at $z/H = 0.5$ for a range of Re. Different Re cases are represented by different symbol shapes, as denoted in the legend.

that the fluid in this region rotates in the direction opposite to the dominant recirculation region and with much reduced velocities. The presence of the low-velocity bubble region is also reflected in the v_θ contour plot by a widening of the gap between contour lines in the near-axis region. It is clear from Figure 7 that the azimuthal circulation is strongly dependent on z/H. In the recirculation zone external to the VB bubble, v_θ decreases as $z/H \rightarrow 1$, while v_r and v_z appear to be less affected. The ratio of v_z/v_θ eventually determines, in part, the formation of VB downstream (Billant et al., 1998).

The extraction of single-dimensional velocity profiles provides an opportunity for an even more detailed analysis of the flow. The v_z and v_θ profiles at an axial position of $z/H = 0.5$ are shown in Figures 8 and 9, respectively. Four cases ($Re = 600$, $Re = 1,000$, $Re = 1,800$, and $Re = 2,600$) are included in order to illustrate the nature in which the flow develops with Re. The cases selected illustrate well the flow profile transitions. The first point to note regarding Figure 8 is that both the maximum and minimum points move radially outward as Re increases. This is indicative of the outer recirculation region distorting as the vortex breakdown region shifts and widens. Secondly, the axial velocity at $r = 0$ gradually moves from positive to negative. The transition from positive to negative corresponds to the detachment of the VB recirculation torus from the central axis (Brøns et al., 2001), leaving a small region of downwards-spiraling fluid which slowly flows downstream into the outer recirculation region. Profiles of normalized azimuthal velocity ($v_\theta/(R\omega)$) at $z/H = 0.5$ are shown in Figure 9. It is clear that the azimuthal 'jet' profile near the sidewall has an Re-dependent shape. As Re increases, the peak v_θ value moves gradually toward the wall and steadily increases in magnitude until $Re \approx 1,800$, at which point the profile becomes more constant. There is also evidence of the VB topology evolution contained within the v_θ profiles, as a second local maximum appears around $r/R = 0.35$ between $Re = 1,000$ and $Re = 1,800$, that is, at a similar point to the 'bubble detachment' evident in Figure 8.

To progress with calculating the principal stresses from the 3D stress tensor T, all nine spatial velocity gradients need to be resolved. Standard SPIV only facilitates the measurement of six of these, those in the r and z directions. To complete T, an assumption must be made regarding the remaining three gradients, that is, those along the azimuthal axis. In a majority of the cases studied, the time-progressive velocity measurements do not appear to present any strong fluctuations in the azimuthal component aside beyond the background noise level, despite the fact that the recording time encompasses multiple disk rotations. It is therefore reasonable to assume that, for the purpose of the stress field estimate, the flow is steady and axi-symmetric over the Re domain. In other words, that the three velocity gradients along the azimuthal axis are negligible in comparison with the six velocity gradients across the field of view. The measured fluctuations provide an upper limit of the Reynolds stresses in the vessel. As expected, these are several orders of magnitude below the mean viscous stresses. This is unsurprising as flows in this vessel configuration with these H/R and Re values fall within the laminar and early transition regimes, rather than the turbulent regime (Brøns et al., 2001; Spohn et al., 1993).

Figure 10 illustrates the distribution of the two major principal stress magnitudes, non-dimensionalized by the

(a)

(b)
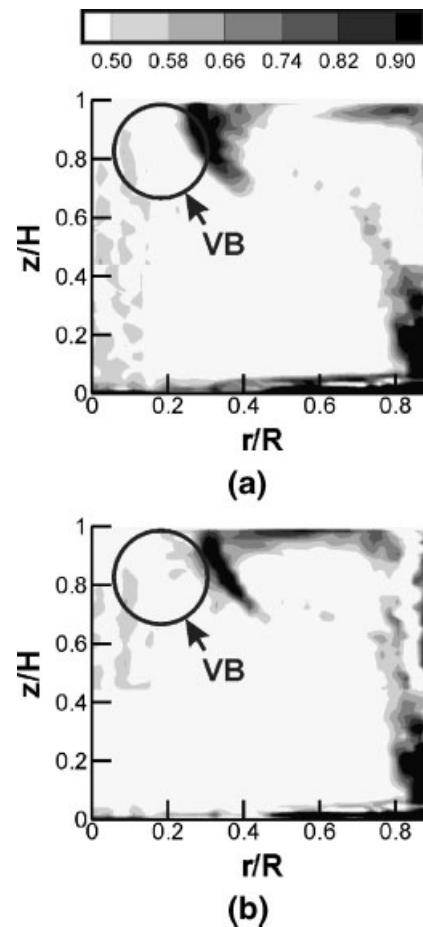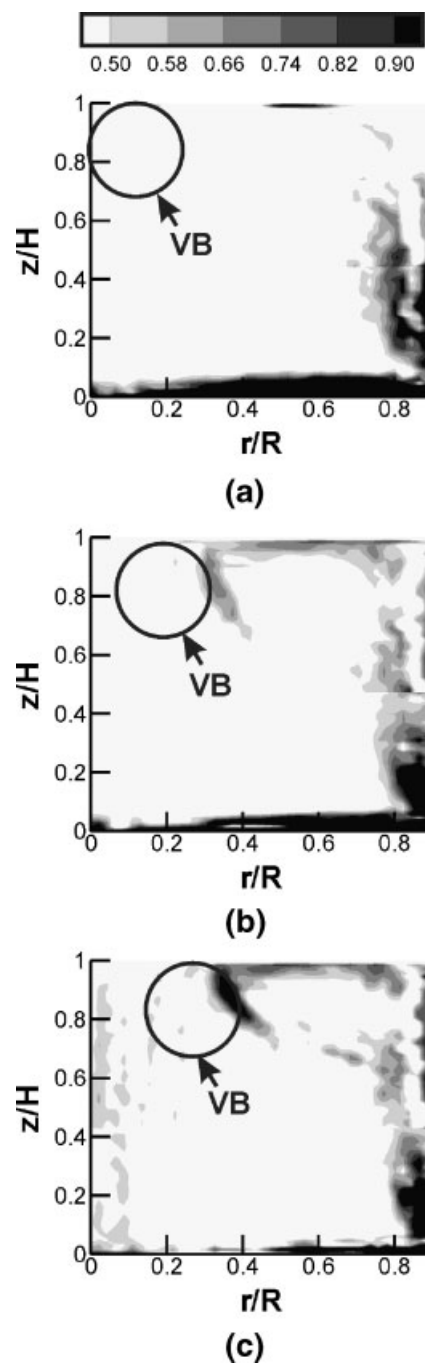
Figure 10. Distribution of (**a**) $\sigma_1/\mu\omega$, and (**b**) $\sigma_3/\mu\omega$, across the entire right-hand side of the meridional plane at $Re = 2,400$. The approximate location of the vortex breakdown recirculation is annotated.

product $\mu\omega$, where μ is dynamic viscosity, at $Re = 2,400$. The entire meridional plane is shown, as results from two separate experiments have been combined into each plot. The slight discontinuity at $z/H \approx 0.4$ indicates the location where the two data sets have been joined. The first principal stress component, σ_1, presented in Figure 10a, corresponds to the negative compressive stress acting on the fluid element, while σ_3, in Figure 10b, represents the positive tensile stress. σ_1 and σ_3 are distributed similarly, yet not identically. The remaining principal stress component, the intermediate component, σ_2, is typically much closer to 0 than σ_1 or σ_3, and has a value determined by the difference $(\sigma_1 - \sigma_3)$. The three principal stresses act along orthogonal axes, the directions of which vary with respect to spatial position in the bioreactor. Due to the fact that the contours of σ_2 do not illustrate significant regions of stress, this component is not included here. Despite σ_3 and σ_1 having different distributions, the two plots have some common features. In particular, in both cases the largest stresses seem to be located in three regions—along the surface of the disk, along the cylinder sidewall, and along the boundary of the VB bubble. For cell and tissue culture applications, the shear stresses are particularly important. Different shear stresses act along the different planes (i.e., r–z, r–θ, and z–θ), however, the peak σ_1 and σ_3 regions also indicate the regions of maximum shear stress.

As with most other impeller-driven bioreactors (see Doran (1999)), high stresses are induced in the vicinity of the impeller. In the current vessel, the maximum stresses occur at the perimeter of the impeller, where the fluid being spun radially outward is turned abruptly upward by the cylinder wall, coinciding with the occurrence of an azimuthal jet. The high stresses along the side and bottom surfaces are the result of boundary layer shearing. This shearing is weaker along the upper portion of the sidewall, where much of the strong azimuthal and axial momentum has been dispersed, and near the free-surface, which does not have a 3D no-slip condition. The stress peak at the boundary of the VB bubble is caused by the considerable difference in conditions either side of the interface between the opposite rotating recirculation regions. The strong spatial gradients in the dominant velocity component, v_θ, further contribute to the stresses in this region.

Within the center of the vortex breakdown region, the stresses are substantially lower than the peak stress region. Particles or cells trapped within a VB bubble are subjected to a consistent, low-magnitude stress, whereas particles or cells trapped in the outer recirculation region are subjected to a greater variety of stress conditions. They also experience a much higher peak stress, which occurs as they travel past the Ekman layer and through the bottom corner of the cylinder.

Much of the normalized stress field in the $Re = 2,400$ example is similar at other Re; however, the distribution in the vicinity of the VB region exhibits some Re-dependency. A high stress region is consistently located along the upper edge of the bubble, however, because the VB region geometry changes with Re, so too does this stress region. In Figure 11, σ_3 contours are plotted at $Re = 1,000, 1,600$, and $2,800$. Once

Figure 11. Distribution of $\sigma_3/\mu\omega$ across the entire right-hand side of the meridional plane at (**a**) $Re = 1,000$, (**b**) $Re = 1,600$ and (**c**) $Re = 2,800$. The approximate location of the vortex breakdown recirculation is annotated in each case.

again, the cases selected are those that best illustrate the transition with respect to Re. Despite being time-averaged data, the σ_3 contours are fairly noisy due to the processing required to compute the principal stress values, in particular the calculation of spatial gradients and then the reduction of T to its eigenvectors. However, the plotted contours show a consistent and distinct pattern that evolves as Re increases in a manner related to changes in flow topology. At $Re = 1,000$, where the VB region is limited to low r/R, the high stress band

is closer to the central axis than the other cases, and is of such low magnitude as to be not detectable in Figure 11. As Re increases, the VB boundary high stress region moves radially outward and becomes more slanted, reflecting a change in the outer bubble geometry. There is also a consistent increase in the magnitude of the peak stresses in this region, which is indicative of an increase in the ratio of the velocities outside the bubble, to those inside. It should be noted that the peak σ_3 regions near the bottom and side surfaces do not change their geometry, but appear to become more intensified with Re.

Flow in Tissue-Engineering Bioreactors

VB bubble formation occurs with any one of the three scaffold models submerged in the cylinder at a location between $0.5 \leq z/H \leq 1.0$ on the central axis. Furthermore, changing Re from 1,200 to 2,400 produces an alteration in the shape of the VB bubble which is similar to the alteration which occurs without disks present. Nevertheless, the presence of disks does result in a different steady flow topology to the disk-free case. In general, bubble regions containing an enclosed stationary scaffold have a larger outer diameter than those that do not. The precise change in VB geometry caused by submerging stationary circular disks in the cylinder is dependent on the size, (indicated by radius r_s/R), and location, (r/R, z/H), of the disks. The general manner in which disks of different size control bubble topology is apparent from the visualization images presented in Figure 12. These images each capture the flow at a point in time where it is fully developed and the majority of the tracer particles, which have a specific gravity 1.05 times that of water, have been separated to the outer recirculation region. The $r_s/R = 1/13$ scaffold, shown in Figure 12a, is fully enclosed in the VB bubble; yet, it does not appear to greatly effect the internal recirculation. For case (b), $r_s/R = 2/13$, the scaffold is fully enclosed in the bubble, however, the shape of the bubble is more distorted than case (a). For (c), $r_s/R = 3/13$, the diameter of the disk extends to the boundary of the bubble. Upstream of the disk the bubble is distorted in a manner similar to case (b); however, downstream of the disk the bubble geometry is profoundly different. Here, the bubble spirals around the outside of the disk and joins a spiral column leading down around the central axis to the rotating bottom. Once the flow is fully developed, this spiral structure is steady in 3D space. Repeated experiments produce different angular orientations of the spiral, indicating that the bubble/column asymmetry may be initiated by asymmetries in the disk alignment rather than the rig. A displacement of the scaffold in the positive r or z directions tends to shift the bubble the same way.

Figure 13 contains the meridional, in-plane vector field for the case where the large scaffold ($r_s/R = 3/13$) is located at (r/R, z/H) = (0, 0.7), causing significant disruption to the breakdown bubble. The region occupied by the support column and disk has been blanked out, as has the region obscured to the left hand camera by the front of the disk. As the SPIV images were affected by specular reflection off the

(a)

(b)

(c)
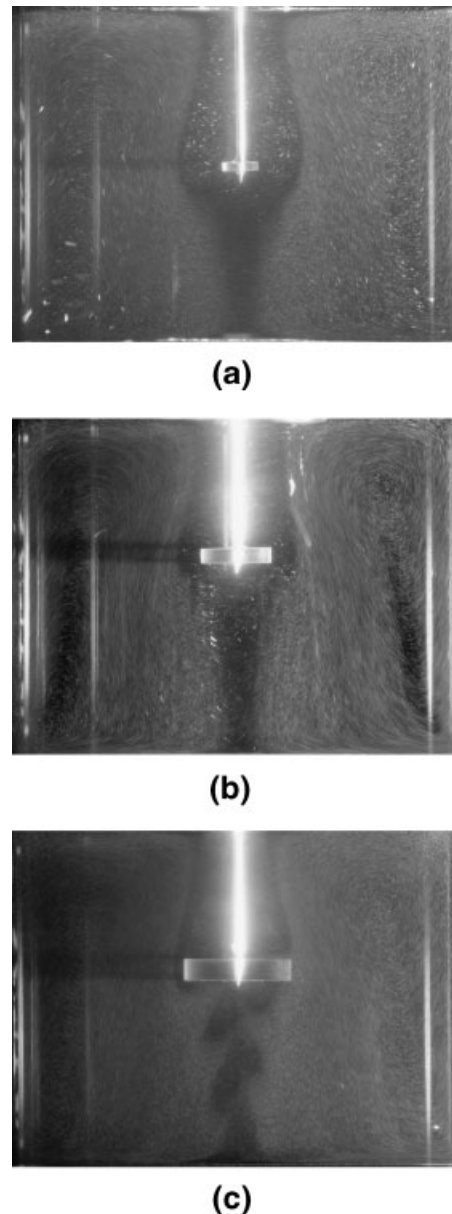
Figure 12. Lamp-illuminated particle visualization of meridional plane flow for (**a**) $r_s/R = 1/3$, (**b**) $r_s/R = 2/13$, and (**c**) $r_s/R = 3/13$. In all cases $Re = 1,200$, and the center of the scaffold is at (r/R, z/H) = (0, 0.5).

submerged surfaces, parts of the fluid region surrounding the support column and disk have also been omitted. Despite the presence of bluff bodies that take up a significant proportion of the VB volume, the internal recirculation still occurs, but is compressed into a small region between the upper surface of the disk and the free surface. Below the disk, the fluid is nearly quiescent—the vectors are smaller, even, than those in the bubble region above the disk. Comparison between Figures 13 and 6 provides an illustration of the typical changes caused to the meridional vector field by the placement of a scaffold on the central axis. The same vector scaling and Reynolds number (1,200) were used for both cases. The magnitude and direction of viscous stresses acting along the scaffold surface were estimated from the velocity
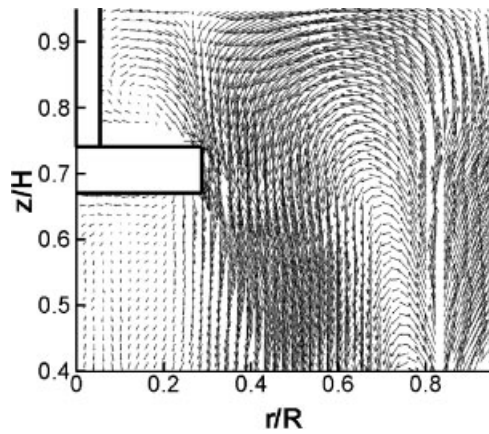
Figure 13. Two-dimensional (v_r, v_z) vector field in the vicinity of a scaffold of size $r_s/R = 3/13$ located at $z/H = 0.7$, with $Re = 1,200$.

measurements in the rows surrounding the disk. Figure 14 represents the σ_3 distribution corresponding to the vector field presented in Figure 13. The surface of the disk closest to the boundary of the VB region experiences much higher local stress levels than the surfaces adjacent to the upstream VB region or the downstream low velocity vortex region. The stresses near the r_s/R edge appear to be particularly high because the disk juts into the VB interfacial region, which contains relatively high stress even without the presence of scaffolds. In addition, the presence of a scaffold model forces the axial flow to diverge abruptly around its edge, leading to higher deformation stresses. Therefore, the edge stresses can be reduced by ensuring that the scaffold does not jut into the VB boundary region. This can be accomplished by reducing the r_s/R diameter ratio, by carefully considering the axial placement of the scaffold, and by ensuring that the scaffold remains on or very near the central axis.

DISCUSSION

This study provides an introductory demonstration of how advanced experimental fluid dynamics may be employed to
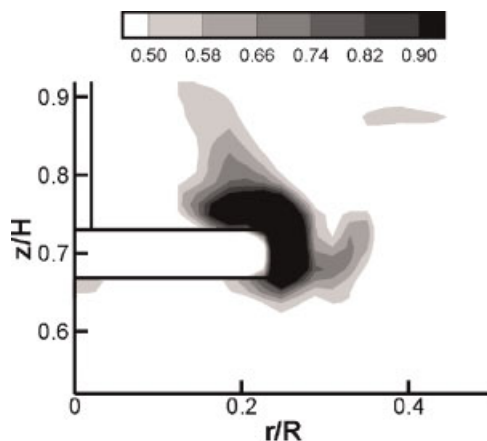
Figure 14. Local distribution of $\sigma_3/\mu\omega$ around a scaffold of size $r_s/R = 3/13$ located at $z/H = 0.7$, with $Re = 1,200$.

quantify flows for cell culture applications. The bioreactor flow chosen for this study was that within a cylinder with a free-surface and rotating bottom, as such a flow provides low shear, laminar mixing at the Re values considered. This geometry, while being novel for cell culture purposes, is a simplification of other stirred cylinder bioreactors, such as the spinner flask and the rotating wall perfused vessel, and so remains a feasible design. Indeed, the results of this study need not be considered in isolation from these other designs, as many of the issues associated with this flow, such as the impeller shear layer, the sidewall shear layer, the separate mixing regions, and the 3D nature of the flow, are also relevant to the aforementioned vessels.

Qualitative (Laser-Particle Visualization) and quantitative (SPIV) techniques were used to study the flow under conditions representative of freely suspended cell culture and stationary-suspended scaffold/bioreactor systems. For freely suspended cell or microcarrier culture, flows at Re below that for the onset of vortex breakdown may not have the momentum to provide adequate mixing or to suspend the cell aggregates for long periods of time. For instance, at $Re = 600$, it was observed through flow velocimetry that the fluid above $z/H \approx 0.70$ was nearly quiescent. As Re increases, the disk rotation becomes sufficient to cause circulation through the axial and meridional planes. Above a certain threshold ($Re > 780$ for $H/R = 1.5$), the on-axis vortex breakdown bubble appears on the central axis, albeit small at first. With an increase in Re, both the size and geometry of this region change. It appears possible, when considering the entrainment of particles in the VB region during flow visualization that this region may provide suitable conditions for cell culture within an environment isolated from the remainder of the fluid volume.

The principal stress fields indicate that retainment of suspended cell aggregates in the VB region would be desirable for cell or tissue cultures that require mixing for nutrient transport, but for which exposure to large stresses or stress gradients would be particularly damaging. 3D stresses peak at the interface between the rotating lid and the cylinder wall, and are relatively high near the bottom (Ekman) boundary layer and the side (Stewartson) boundary layer. Cells suspended within the large, outer recirculation region are likely to encounter both these high stress regions as they spiral around the central axis toward $z/H \rightarrow 0$, then get accelerated radially and azimuthally by the Ekman pumping mechanism, before being abruptly turned in the positive axial direction by the sidewall. Due to the relatively high velocities in the outer recirculation region, aggregates suspended in this zone are more likely to collide with the impeller or the cylinder sidewall. In contrast, our results indicate that suspensions within the VB region would be exposed to lower stress levels than those outside the VB region, but would nevertheless receive mixing through the internal bubble circulation and advection phenomena reported elsewhere in the literature (Sotiropoulos et al., 2001). In addition, the distance of the centrally located VB region from the impeller or wall prevents collision from

being a major issue. For all *Re* considered in this study, a high stress zone is located at the interface between the upper VB region and the outer recirculation region; however, the size and intensity of this region is less than the aforementioned peak regions. Moreover, as this stress band separates two distinct regions, it is unlikely to be crossed by cell or tissue suspensions. As VB flows are shown to provide a low shear mixing environment, the results of this investigation indicate that the use of VB for suspension culture warrants further study.

The addition of circular disk-shaped scaffold models to the flow did not destroy the VB formations. On the contrary, the bubbles appeared steady and robust, although the geometry was modified depending on the size and position of the submerged scaffold. A disk of size $r_s/R = 1/13$ placed on the central axis could sit comfortably within the VB region. In a dimensionalized system, this disk size is equivalent to a 5 mm diameter scaffold in a 65mm diameter flask, which is similar to the diameter ratio used by Vunjak-Novakovic et al. (1998), although they used multiple scaffolds located off the axis of symmetry. The surface stresses under these conditions are of relatively low magnitude; however, it has been demonstrated that when a larger disk is used (e.g., $r_s/R = 3/13$), the edge of the disk can interfere with the VB boundary, which can cause high local stress. If the disk juts into the interfacial region, the VB recirculation is compressed into the region just above the disk, and the downward axial flow is forced to diverge around the scaffold, leading to large edge stresses. In addition, the region directly below the scaffold becomes nearly stagnant, which may potentially lead to insufficient mixing and/or shear conditions.

Given the assumption of negligible azimuthal gradients, it is worth considering that symmetry breaking has been reported both experimentally and numerically for $Re = 1,910$ at $H/R = 2.0$, although initially the perturbations associated with the instability are not particularly energetic (Hirsa et al., 2002; Lopez et al., 2004). However, for the sake of our current investigation into potential bioreactor flows, quantification of any errors caused by azimuthal fluctuations at higher Reynolds numbers is difficult without the acquisition of further measurements using a different experimental technique. There are some fluctuations in the measurements, however, at this level the fluctuations would be unlikely to cause significant Reynolds stresses, and so are not likely to greatly affect cell culture.

Aside from the potential for vortex breakdown, the flow studied here has several advantages. Firstly, it is laminar, and therefore does not have the strong random component of highly turbulent velocity fields. Secondly, it is approximately axi-symmetric and steady at *Re* values below approximately 2,000. Axi-symmetry is significant in the context of bioreactor flow analysis, as it means that the process of characterizing relevant parameters is greatly simplified. For example, when an axi-symmetric flow is in the steady, time-invariant regime, the stress field is a function of (r, z). In contrast, for a turbulent mixing vessel such as a spinner-flask bioreactor, the stress field is a function of (r, z, θ, t), where t represents the time domain. Laminar flow bioreactors are also simpler to scale up than turbulent tanks, as scaling of turbulent vessels requires an additional scaling of the small-eddy length and energy dissipation.

There are, however, some potential issues associated with a laminar mixing flow. The motion of cell aggregates or microcarrier beads may not be predictable by Eulerian fluid mechanics if their density exceeds a certain threshold. Indeed, as with all suspension bioreactors, the specific gravity should match that of the fluid medium as closely as possible in order to prevent the suspensions from floating to the surface or sinking to the vessel floor. Body forces are particularly important if cells are to be retained within the VB region. In addition, the issue of oxygen diffusion has not been addressed as part of this study. Whether the flow provides adequate oxygen transport is a question that may require further investigation on the basis of individual applications, however, it should be noted that the vessel configuration provides scope for injection of materials at the free surface.

Significantly, the work presented in this article is a demonstration of a novel approach of analyzing rotating flows in a manner which is relevant to the engineering of cell culture bioreactors. Three-component flow measurement has been applied to a bioreactor design scenario, allowing the derivation of 3D stress fields in adequate detail. This is significant as stress levels deserve to receive major consideration in bioreactor design. The few previous studies that have attempted to quantify the stresses within the mixed-flask style of bioreactor have mostly done so by defining a constant to indicate an average shear stress magnitude throughout the vessel over an indefinite period of time (Croughan et al., 1987; Sinskey et al., 1981; Vunjak-Novakovic et al., 1996). The usefulness of this approach seems limited when one considers the spatially, and often temporally, heterogeneous nature of these flows. More recently, the development of computational and experimental techniques has enabled the prediction and measurement of shear-stress components in a two-dimensional plane. Sucosky et al. (2004) measured two-dimensional flow fields around scaffolds within their experimental model of a bioreactor flow agitated by a magnetic-stirrer, and obtained time-variant wall and Reynolds shear stress data.

Even still, the shear stress components measured in a two-dimensional plane fail to provide a complete picture when the flow has three varying velocity components, particularly if the co-ordinate system is chosen arbitrarily. In such flows, all the information pertaining to the viscous stress acting on an element in the bulk flow is contained within the 3D deformation stress tensor, *T*, and so the stress data needs to be presented in a manner which best reflects this tensor. In this article, we chose to present the principal stresses acting on each element, despite the fact that the direction of the principal axes is spatially variable, as these provide a more accurate description of the stresses experienced by cells than shear stresses measured along arbitrarily defined axes. It is worth noting that the shear stresses acting in any plane can be resolved from the three principal stress vectors using simple

geometry. Regions of maximum shear stress coincide with regions of maximum σ_1 and σ_3.

Clearly, the cases presented in this article constitute only a small subset of the rotating lid parameter space. The aspect ratio of 1.5 is close to that of other bioreactors in the literature, however, it may be preferable to choose a lower H/R, so that VB can be initiated at a lower Re. Alternatively, it may be beneficial to use a larger H/R, where multiple breakdown bubbles have previously been observed. Furthermore, there is plenty of scope available for modifying the number and position of submerged scaffolds, and this is currently being investigated by the authors. Finally, it may be desirable to analyze the effect of rig adjustments on the VB geometry and the principal stresses—for instance, the addition of a gas sparger to the system.

The stress and velocity fields have been presented in dimensionless form in this article, in order to emphasize that bioreactors can and should be categorized in such a way that the results have a general relevance, rather than being particular to a certain set of parameter values. Such an approach will make it easier to predict the performance of bioreactor designs under scaled conditions, and eventually to optimize the design of bioreactors on the basis of, say, the mean stress or the oxygen transfer coefficient. For example, it is possible to increase the absolute stress levels while keeping a consistent flow topology by increasing ω but keeping Re constant. The engineer must take care when scaling bioreactors based on Re, to not overlook other factors that may become important. For example, increasing the vessel size will require a slow rotational speed, (as ω scales with R^{-2}), which may in turn lead to practical issues or overly small deformation stresses. In addition, the applicability of the flow models may become Froude number or hydrostatic pressure limited in very large tanks. A solution to this could be to scale out to multiple smaller bioreactors rather than use a single, scaled up bioreactor.

As a final point, while our macroscopic, generalist approach provides meaningful results, there is a need for future work to link closer to the cell-scale biomechanics. The dearth of knowledge regarding how cells respond to stresses is currently being addressed by researchers in many different fields of cellular engineering, however, further progress is needed before the approach to bioreactor design presented here is to be of maximum benefit.

References

Begley CM, Kleis SJ. 2000. The fluid dynamic and shear environment in the NASA/JSC rotating-wall perfused vessel bioreactor. Biotechnol Bioeng 70:32–40.

Begley CM, Kleis SJ. 2002. RWPV bioreactor mass transport: Earth-based and in microgravity. Biotechnol Bioeng 80:465–476.

Billant P, Chomaz JM, Huerre P. 1998. Experimental study of vortex breakdown in swirling jets. J Fluid Mech 376:183–219.

Botchwey EA, Pollack SR, Levine SM, Johnston ED, Laurencin CT. 2004. Quantitative analysis of three-dimensional fluid flow in rotating bioreactors for tissue engineering. J Biomed Mater Res 69:205–215.

Brøns M, Voigt LK, Sørensen JN. 2001. Topology of vortex breakdown bubbles in a cylinder with a rotating bottom and a free surface. J Fluid Mech 428:133–148.

Carrier RL, Papadaki M, Schoen FJ, Bursac N, Langer R, Freed LE, Vunjak-Novakovic G. 1999. Cardiac tissue engineering: Cell seeding, cultivation parameters, and tissue construct characterization. Biotechnol Bioeng 64:580–589.

Cherry RS, Papoutsakis ET. 1986. Hydrodynamic effects on cells in agitated tissue culture reactors. Bioprocess Eng 1:29–41.

Croughan MS, Hamel J-F, Wang DIC. 1987. Hydrodynamic effects on animal cells grown in microcarrier cultures. Biotechnol Bioeng 24:130–141.

Curran SJ, Black RA. 2004. Quantitative experimental study of shear stresses and mixing in progressive flow regimes within annular-flow bioreactors. Chem Eng Sci 59:5859–5868.

Darling EM, Athanasiou KA. 2003. Articular cartilage bioreactors and bioprocesses. Tissue Eng 9:9–26.

Doran PM. 1999. Design of mixing systems for plant cell suspensions in stirred reactors. Biotechnol Prog 15:319–335.

Escudier MP. 1984. Observations of the flow produced in a cylindrical container by a rotating endwall. Exp Fluids 2:189–196.

Escudier MP. 1988. Vortex breakdown: Observations and explanations. Prog Aerosp Sci 25:189–229.

Freed LE, Vunjak-Novakovic G. 1995. Cultivation of cell-polymer tissue constructs in simulated microgravity. Biotechnol Bioeng 46:306–313.

Freed LE, Vunjak-Novakovic G. 2000. Tissue engineering bioreactors. In: Lanza RP, Langer R, Vacanti J, editors. Principles of tissue engineering. San Diego, USA: Academic Press. pp 143–156.

Goodwin TJ, Prewett TL, Wolf DA, Spaulding GF. 2003. Reduced shear stress: A major component in the ability of mammalian tissues to form three-dimensional assemblies in simulated microgravity. J Cell Biochem 51:301–311.

Hall MG. 1972. Vortex breakdown. Annu Rev Fluid Mech 4:195–217.

Hart DP. 2000. PIV error correction. Exp Fluids 29:13–22.

Hirsa AH, Lopez JM, Miraghaie R. 2002. Symmetry breaking to a rotating wave in a lid-driven cylinder with a free surface: Experimental observation. Phys Fluids 14:L29–L32.

Humphrey JD. 2001. Stress, strain and mechanotransduction in cells. J Biomech Eng 123:638–641.

Ishizuka S. 2002. Flame propagation along a vortex axis. Progr Energy Combustion Sci 28:477–542.

Kallos MS, Reynolds BA, Vescovi AL, Behie LA. 1998. High cell density growth of mammalian neural stem cells as aggregates in bioreactors. In: Fan LS, Knowlton TM, editors. Fluidization. New York: Engineering Foundation. pp 653–660.

Kleis SJ, Schreck S, Nerem RM. 1990. A viscous pump bioreactor. Biotechnol Bioeng 36:771–777.

Lawson NJ, Wu J. 1997. Three-dimensional particle image velocimetry: Experimental error analysis of a digital angular stereoscopic system. Meas Sci Technol 8:1455–1464.

Leckie F, Scragg AS, Cliffe KC. 1991. Effect of bioreactor design and agitator speed on the growth and alkaloid accumulation by cultures of catharanthus roseus. Enzyme Microb Technol 13:296–305.

Lopez JM, Marques F. 2004. Mode competition between rotating waves in a swirling flow with reflection symmetry. J Fluid Mech 507:265–288.

Lopez JM, Marques F, Hirsa AH, Miraghaie R. 2004. Symmetry breaking in free-surface cylinder flows. J Fluid Mech 502:99–126.

Martin I, Wendt D, Heberer M. 2004. The role of bioreactors in tissue engineering. Trends Biotechnol 22:80–86.

Nielsen LK. 1999. Bioreactors for hematopoietic cell culture. Annu Rev Biomed Eng 1:129–152.

Niklason LE, Gao J, Abbott WM, Hirschi KK, Houser S, Marini R, Langer R. 1999. Functional arteries grown in vitro. Science 284:489–493.

Prasad AK. 2000. Stereoscopic particle image velocimetry. Exp Fluids 29:103–116.

Raffel M, Willert CE, Kompenhans J. 1998. Particle Image Velocimetry: A Practical Guide. Berlin, Germany: Springer.

Sarpkaya T. 1971. On stationary and travelling vortex breakdowns. J Fluid Mech 45:545–559.

Shachar M, Cohen S. 2003. Cardiac tissue engineering, ex-vivo: Design principles in biomaterials and bioreactors. Heart Fail Rev 8:271–276.

Sinskey AJ, Fleischaker RJ, Tyo MA, Giard DJ, Wong DJC. 1981. Production of cell-derived products: Virus and interferon. Ann N Y Acad Sci 369:47–59.

Soloff SM, Adrian RJ, Liu Z-C. 1997. Distortion compensation for generalized stereoscopic particle image velocimetry. Meas Sci Technol 8:1441–1454.

Sotiropoulos F, Ventikos Y. 2001. The three-dimensional structure of confined swirling flows with vortex breakdown. J Fluid Mech 426:155–175.

Sotiropoulos F, Ventikos Y, Lackey TC. 2001. Chaotic advection in three-dimensional stationary vortex breakdown bubbles: Sil'nikov's chaos and the devil's staircase. J Fluid Mech 444:257–297.

Sotiropoulos F, Webster DR, Lackey TC. 2002. Experiments on Lagrangian transport in steady vortex-breakdown bubbles in a confined swirling flow. J Fluid Mech 466:215–248.

Spohn A, Mory M, Hopfinger EJ. 1993. Observations of vortex breakdown in an open cylindrical container with a rotating bottom. Exp Fluids 14:70–77.

Sucosky P, Osorio DF, Brown JB, Neitzel GP. 2004. Fluid mechanics of a spinner-flask bioreactor. Biotechnol Bioeng 85:34–46.

Thompson MC, Hourigan K. 2003. The sensitivity of steady vortex breakdown bubbles in confined cylinder flows to rotating lid misalignment. J Fluid Mech 496:129–138.

Venkat RV, Stock R, Chalmers JJ. 1996. Study of hydrodynamics in microcarrier culture spinner vessels: A particle tracking velocimetry approach. Biotechnol Bioeng 29:456–466.

Vunjak-Novakovic G, Freed LE, Biron RJ, Langer R. 1996. Effects of mixing on the composition and morphology of tissue-engineered cartilage. Am Inst Chem Eng J 42:850–860.

Vunjak-Novakovic G, Obradovic B, Bursac P, Martin I, Langer R, Freed LE. 1998. Dynamic cell seeding of polymer scaffolds for cartilage tissue engineering. Biotechnol Prog 14:193–202.

Willert C. 1997. Stereoscopic digital particle image velocimetry for application in wind tunnel flows. Meas Sci Technol 8:1465–1479.

Williams KA, Saini S, Wick TM. 2002. Computational fluid dynamics modeling of steady-state momentum and mass transport in a bioreactor for cartilage tissue engineering. Biotechnol Prog 18:951–963.

Wu F, Dunkelman N, Peterson A, Davisson T, la Torre R, De Jain D. 1999. Bioreactor development for tissue-engineered cartilage. Ann N Y Acad Sci 875:405–411.